Infrared and Terahertz Synchrotron Radiation: Optics and Applications

Shin-ichi Kimura

UVSOR Facility, Institute for Molecular Science, and School of Physical Sciences, The Graduate University for Advanced Studies, Okazaki 444-8585, Japan
`kimura@ims.ac.jp`

1 Introduction

One method for creating intense as well as bright terahertz (THz) and infrared (IR) light is by using radiation from relativistically accelerated electrons, such as synchrotron radiation (SR) and free-electron laser (FEL). SR is the radiation emitted from bending-magnets and insertion devices (undulators/wigglers). Because SR consists of broadband electromagnetic waves from the X-ray to the THz range, light with the desired wavelength and intensity (photon flux) can be obtained by using suitable optics. SR is a good source for spectroscopy, and over 20 SR facilities worldwide are equipped with IR/THz beamlines. In contrast, FEL is monochromatic light with high coherence and relatively high intensity. These properties of FEL make it worthwhile as an excitation source and as monochromatic probing light.

The size of the SR light source is determined by the size of the electron beam in the accelerator. The electron beam size is similar to the wavelength of THz light (i.e. sub millimeter size). Because the emission angle of SR is small, the electron beam emittance (i.e. the area occupied by the particles of the beam in space and momentum phase space) is smaller than that of the THz light. The SR light can therefore be focused down to spot size, with an ideal diffraction limit. This property makes the light suitable for microscopic spectroscopy (micro-spectroscopy). In fact, the purpose of almost all of the world's IR/THz beamlines is micro-spectroscopy and micro-imaging with higher spatial resolution than with conventional IR microscope.

In the case of SR light sources, the emission point is located in a vacuum chamber with a bending magnet. Since the vertical space available for collecting the SR is narrow, all of the emitted light cannot be collected. If we have a very wide horizontal acceptance angle, the emission point becomes an emission arc. Therefore, laboratory optics cannot be utilized with IR/THz SR. In addition, the emission point in an electron accelerator is in an ultra-high vacuum ($\sim 10^{-8}$ Pa), whereas THz light needs a pressure of less than 1 Pa for excluding the absorption of water vapor. To separate the ultra-high vacuum of

the accelerator and the low vacuum of the downstream optics, optical windows are used. Because SR light is more broadband than that from conventional THz/IR light sources, the use of optical windows restricts the wavelength regions available. To optimize the use of the wide wavelength region of SR, exchange of optical windows without breaking the vacuum is effective.

In Japan, there are currently three IR/THz beamlines. The first IR/THz beamline, BL6A1, has been constructed at UVSOR in 1986. [1] In 2003, UVSOR was upgraded to the lowest emittance ring (27 nm rad) among small SRs, with an acceleration energy below 1 GeV and its name was changed to UVSOR-II. [2] Simultaneously, BL6A1 was upgraded to the new IR/THz beamline, BL6B, with high brilliance and high flux [3]. To obtain higher performance, we employed a so-called "magic mirror" with a large acceptance angle (215(H) × 80(V) mrad^2) [4]. Upgrading the beamline made the photon flux of BL6B four times larger, and the brilliance 10^2 times larger, than those of BL6A1. In 1999, another IR beamline was constructed at SPring-8 (in Hyogo Prefecture, Japan) [5], which is the largest SR ring in the world. The beamline was equipped with a three-dimensional magic mirror for the first time. At SPring-8, spectroscopy at high temperature and high pressure are used to investigate conditions inside the Earth. Spectroscopy of correlated materials at low temperature and high pressure is also performed. In 2009, a new IR micro-spectroscopy beamline was constructed at the small SR ring, AURORA, at Ritsumeikan University. [6] The beamline will be dedicated to industrial use.

To perform IR/THz spectroscopy using SR, special optics that differ from those used in laboratory systems are needed. In this paper, the IR/THz optics developed for use with SR are introduced, as in an example of their application using IR/THz SR.

2 Principle of three-dimensional magic mirror optics for THz/IR SR

SR is characterized by the emission angle of light. When a relativistic electron beam moves in an external field, the radiation spectrum ($\partial^2 P(\omega)/\partial\omega\partial\Omega$) from a minute orbital is [7]

$$\frac{\partial^2 P(\omega)}{\partial\omega\partial\Omega} = \frac{e^2}{12\pi^3\varepsilon_0 c}\left(\frac{\omega\rho}{c}\right)^2\left(\frac{1}{\gamma}+\theta^2\right)\times\{K_{2/3}^2(\xi)+\frac{\gamma^2\theta^2}{1+\gamma^2\theta^2}K_{1/3}^2(\xi)\} \quad (1)$$

Here, e is the elemental charge, ε_0 the dielectric constant of the vacuum, c the velocity of light, ρ the orbital radius, and γ the ratio of energy to rest mass. $K_{2/3}(\xi)$ and $K_{1/3}(\xi)$ are modified Bessel functions, and $\xi = \omega R/3c(1/\gamma^2 + \theta^2)^{3/2}$, where R is the radius of the electron orbit. The function corresponds to the vertical distribution of SR in the orbital plane. For instance, the vertical
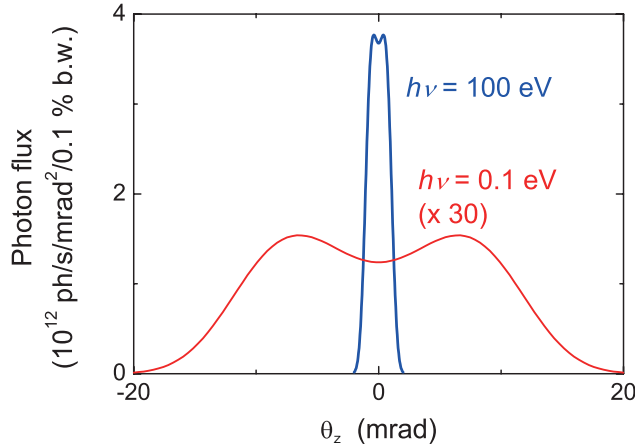
Fig. 1. Vertical distribution of bending-magnet radiation of the UVSOR-II storage ring at photon energies of 0.1 and 100 eV.

emission of the bending-magnet radiation at UVSOR-II is shown in Fig. 1. In the figure, the emission at a photon energy of 100 eV is located around the orbital plane ($\theta_z = 0$ mrad), but the emission of the 0.1-eV photon energy expands above 10 mrad from the orbital plane. The intensity at 0.1 eV is much lower than that at 100 eV. These properties imply that the vertically wide acceptance angle at 0.1 eV is needed for high intensity.

On the horizontal axis, on the other hand, the emission from a minute emission angle is the same as in the above function, but the circular orbit of electron beams made by the Lorentz force due to the presence of the dipole magnet is important. This indicates that SR from the dipole magnet is not an ideal point source, but is instead an arc source. The light cannot be focused to a point by using circular/toroidal mirrors. Thus these mirrors cannot maintain high brilliance.

The "magic mirror" for bending-magnet radiation focused to one point was discovered by Lopez-Delgado and Szwarc in 1976. [8] In this paper, the shape was defined only in the orbital plane. In reality, however, SR is emitted not only in the orbital plane but also to the horizontal axis. We therefore extended the shape of the magic mirror to a three-dimensional one, creating a "three-dimensional magic mirror (3D-MM)," and we installed this mirror in the IR beamline (BL43IR) at SPring-8. [9] SPring-8 is the largest SR ring in the world with an orbital radius of about 40 m. The acceptance angle of 36 mrad corresponds to the emission length of 1.44 m (Fig. 2a). If a toroidal mirror is added to collect the light, then the focal image, calculated by a ray tracing method, is not good (Fig. 3a). This result indicates that the high brilliance of SR cannot be preserved by using a toroidal mirror. We therefore employed the 3D-MM. The following calculations are used to form the 3D-MM:
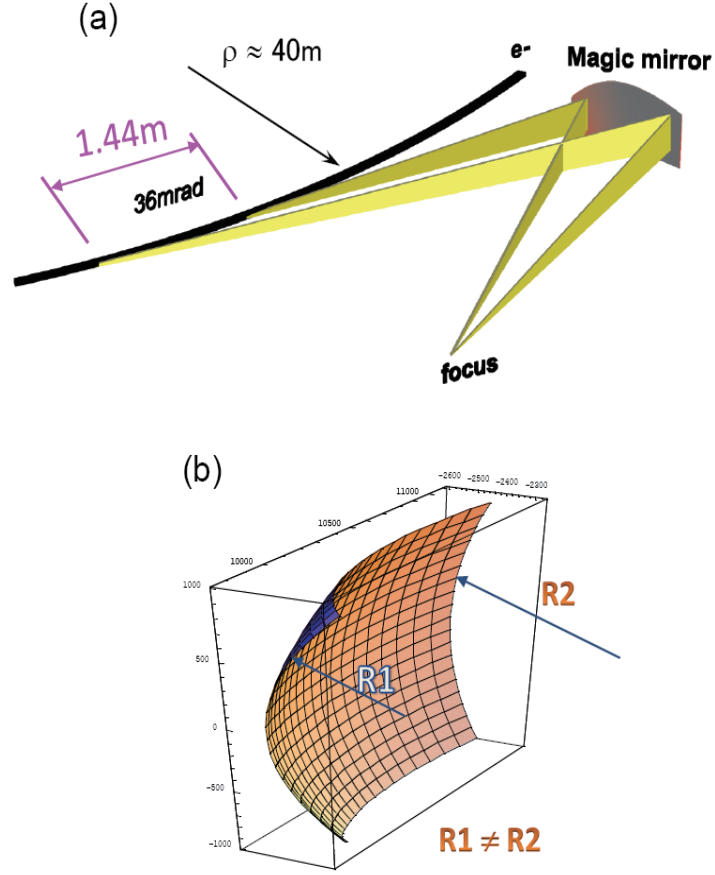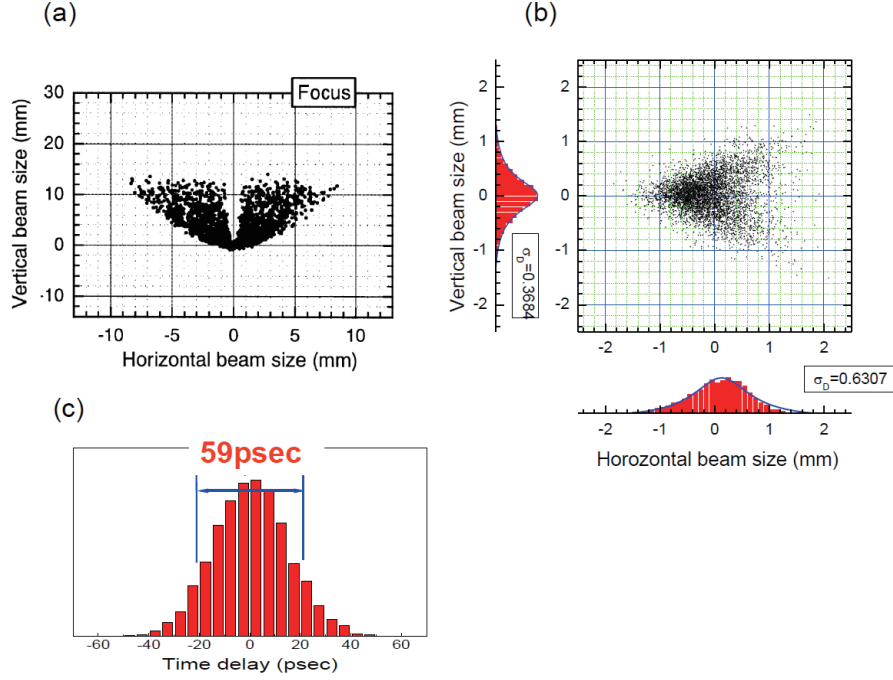
Fig. 2. Schematic figure of the optics using a three-dimensional magic mirror (3D-MM) at BL43IR of SPring-8 (a) and the curvature of the 3D-MM surface (b).

$$\overline{AM}(\theta) = \frac{\frac{1}{2}\{(d_0 - \rho\theta)^2 - \rho^2 a^2\} + a\rho\sin\theta}{d_0 - \rho\theta - a\cos\theta} \tag{2}$$

$$\overline{MI}(\theta) = \sqrt{\rho^2 + \overline{AM}(\theta)^2 + a^2 - 2a(\rho\sin\theta + \overline{AM}(\theta)\cos\theta)} \tag{3}$$

$$R(\theta) = \frac{2\overline{AM})(\theta)(d_0 - \rho\theta - \overline{AM}(\theta)}{d_0 - \rho\theta} \times \cos\{\frac{1}{2}\cos^{-1}\left(\frac{\overline{AM}(\theta) - a\cos\theta}{\overline{MI}(\theta)}\right)\} \tag{4}$$

$$x(\theta,\nu) = \rho\cos\theta - \overline{AM}(\theta)\sin\theta + \frac{|R(\theta)|\{\sin\theta - \frac{\rho\cos\theta - \overline{AM}(\theta)\sin\theta}{\overline{MI}(\theta)}}{\sqrt{2 + \frac{2(\overline{AM}(\theta) - a\cos\theta)}{\overline{MI}(\theta)}}}\{1 - \cos\left(\tan^{-1}\frac{\nu}{R(\theta)}\right)\}$$

$$\tag{5}$$

(a)

(b)

(c)

59psec

Fig. 3. Ray tracing images at the first focus using a toroidal mirror (a) and a three-dimensional magic mirror (b) at BL43IR of SPring-8. (c) Time structure at the focal point, using the three-dimensional magic mirror.

$$y(\theta,\nu) = \rho\sin\theta + \overline{AM}(\theta)\cos\theta + \frac{|R(\theta)|\{-\sin\theta + \frac{a-\rho\sin\theta - \overline{AM}(\theta)\cos\theta}{\overline{MI}(\theta)}}{\sqrt{2 + \frac{2(\overline{AM}(\theta) - a\cos\theta)}{\overline{MI}(\theta)}}}\{1 - \cos\left(\tan^{-1}\frac{\nu}{R(\theta)}\right)\}$$

(6)

$$z(\theta,\nu) = R(\theta)\sin\left(\tan^{-1}\frac{\nu}{R(\theta)}\right)$$

(7)

Here, ρ is the orbital radius of electron beams, a the distance between the center of the electron beam and the focal position, d_0 the optical length from the standard position, θ the acceptance angle of SR, and ν the vertical size of the magic mirror. For instance, the parameters for BL43IR at SPring-8 are as follows; $\rho = 39271.8$mm, $a = 46025.4$mm, $d_0 = 69807.4$mm, $\theta = 1.4804$ to 1.5169 rad, $\nu = -22$ to $+22$ mm. The meanings of $\overline{AM}$, $\overline{MI}$, and R are the same as in ref. [8]. The vertical radius of the magic mirror is obtained for an approximation of a spherical shape by using the distance from the emission point to the focal point.

The shape of a magic mirror surface with the above parameters is shown in Fig. 2b. The surface is very complex because of the non-spherical and non-

**Fig. 4.** Overview of the UVSOR-II storage ring.

symmetric shape. To fabricate the surface, a recently developed numerical cutting method is used.

The focal image calculated by using the ray tracing method is shown in Fig. 3b. The focal size is much smaller than that with the toroidal mirror (see Fig. 3a). The magic mirror cannot only focus SR from the circular electron orbital; it can also reduce the time structure of the emission length to the longitudinal width of the electron bunch (~ 100 ps), because the magic mirror is characterized by a constant distance from the emission point to the focal point including the trajectory of the electron bunch. The calculated time structure is shown in Fig. 3c. In the calculation, the beam length was assumed to be 15 ps. The time structure at the focal point was evaluated to be 59 ps about 4 times longer than the electron beam length.

3 IR/THz beamline optics at UVSOR-II

The 3D-MM was installed in the THz/IR beamline BL6B at UVSOR-II (Fig. 4) in 2004. [3] UVSOR-II is a relatively small SR ring with a circumference of about 53 m and an electron beam bending radius is 2.2 m. If a 3D-MM is introduced into such a small SR ring, a large acceptance angle can be employed. For instance, at UVSOR-II, the acceptance angle became 215 mrad in the horizontal plane and 80 mrad in the vertical plane. The combination of a large acceptance angle and the shape of the 3D-MM gives high brilliance.

The layout and optics of the beam extraction part (front-end) are shown in Figs. 5a and b, respectively. The first mirror in the bending-magnet chamber is
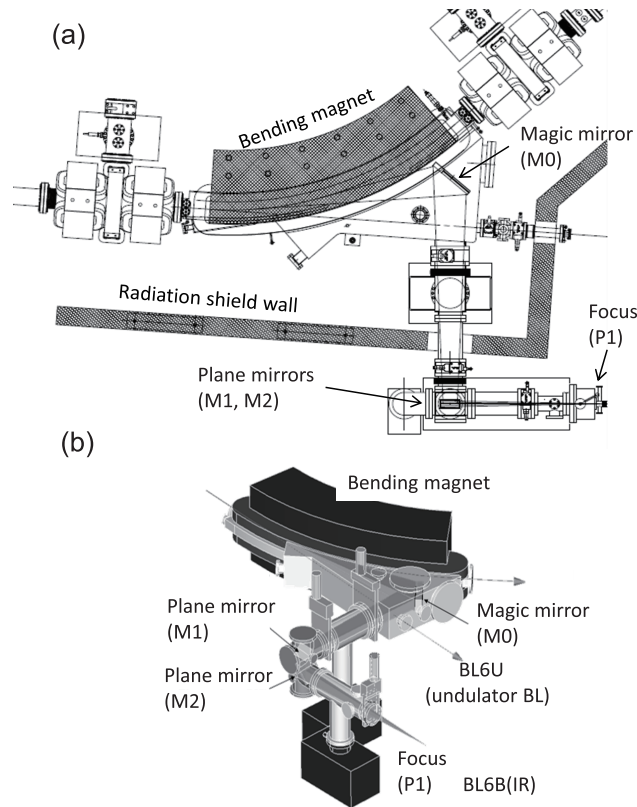
Fig. 5. Top view (a) and 3D view (b) of the front-end optics of BL6B, UVSOR-II.

a magic mirror with dimensions of 300 mm (horizontal) by 100 mm (vertical). A copper pipe (diameter 5 mm) for water cooling is located in the orbital plane in front of the magic mirror to reduce heat load due to the increases photon energy of the SR.

The THz/IR SR extracted by the magic mirror is derived to the first focusing point (P1) by two plane mirrors (M1 and M2). The position and angle of the light can be controlled by M1 and M2 (Fig. 5b). The light emittance of the THz/IR beamline is the product of the light size and the emission angle at P1. The beam size at P1 calculated by the ray-racing method, and the actual beam size obtained, are shown in Figs. 6a and b. The beam in the experimental result is spherical and about 1.2 mm in diameter, in contrast with the elliptical shape of 1×2 mm^2 in the calculation. This is because the calculation was done at a photon energy of 0.1 eV, whereas the experimental result was obtained at a photon energy range of 0.05 to 2 eV by using an HgCdTe (MCT) detector. The result indicates that the SR light can be ideally focused by using the 3D-MM.
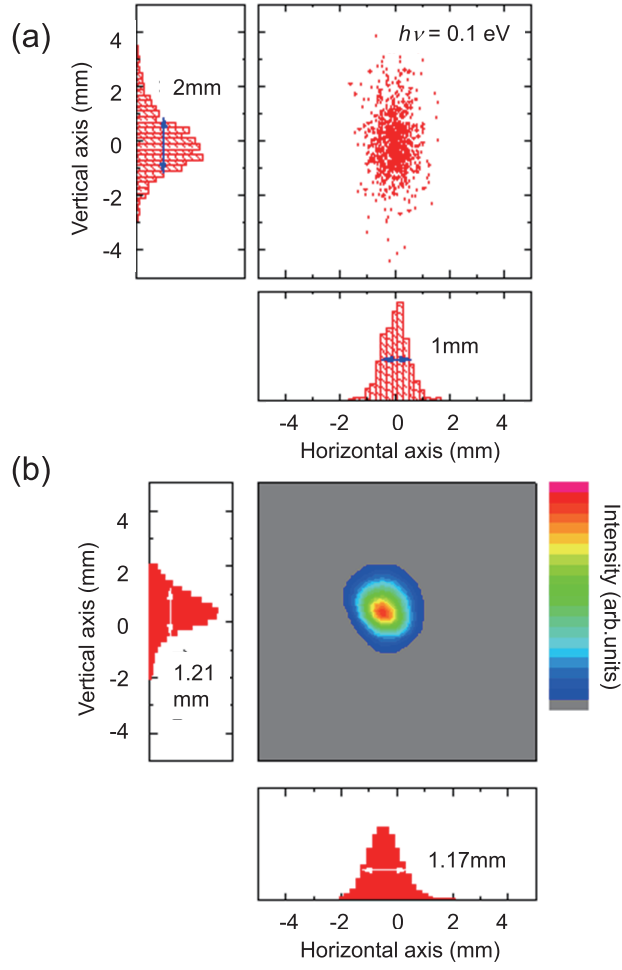
Fig. 6. Ray trace result at the first focal point at a photon energy of 0.1 eV (a) and beam profile measured by using an MCT detector (b) at the first focusing point (P1) in Fig. 5.

The distance from the magic mirror to P1 is 2.5 m and the horizontal solid angle from P1 to the magic mirror is about 86 mrad. By using the experimental beam size at P1, the horizontal emittance at a photon energy of 0.1 eV ($\sigma_x \cdot \sigma_x'$) becomes 52 μm·rad. In the vertical plane, on the other hand, the emission angle ($\sigma_y' \sim 12$ mrad) shown in Fig. 1 at 0.1 eV and the lengths between the center of the emission arc and the magic mirror (about 1 m) and between the magic mirror and P1 (about 2.5 m) make the emittance ($\sigma_y \cdot \sigma_y'$) 5.4 μm·rad. The emittance of a conventional IR spectrometer is $\sigma_{x,y} \cdot \sigma_{x,y}' = 200$
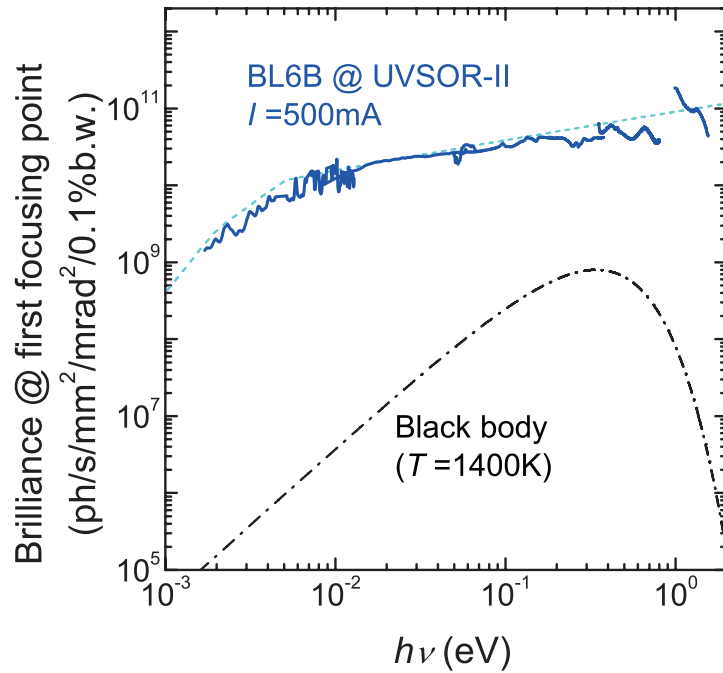
Fig. 7. Calculated (dashed line) and experimentally obtained (solid line) brilliance of BL6B, UVSOR-II compared with those of a thermal (black body) light source at $T = 1400$ K (dash-dotted line).

to 1000 μm·rad. This implies that SR light has a much lower emittance than conventional laboratory sources.

This low emittance gives high brilliance. In fact, in terms of black body emission at 1400 K, the brilliance of BL6B at UVSOR-II is several orders of magnitude greater than that of a conventional source (Fig. 7). The difference in the THz photon energy region below 50 meV is much larger than that in the IR region above 50 meV. This indicates that the light is suitable for micro-spectroscopy in the THz region.

4 IR/THz beamline optics at UVSOR-II

The BL6B IR/THz of UVSOR-II covers the range of 0.5 meV to 2 eV (4 to 16 000 cm^{-1}) by using two Fourier transform IR interferometers (FTIRs). One is a Martin-Puplett-type (MP) interferometer (FARIS-1, Jasco Inc.) that covers a photon energy range of 0.5 to 10 meV. The other is Michelson-type interferometer (MI) (Vertex 70v, Bruker Inc.) covering 5 meV to 2 eV and with four beam splitters (Mylar 23 μm, Mylar 6 μm with multilayer coating,
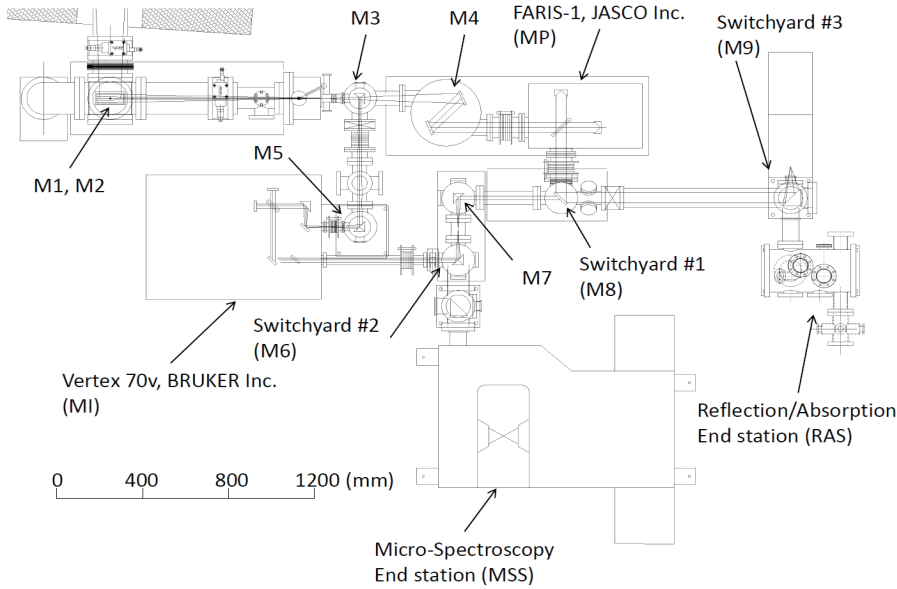
Fig. 8. Layout of the beam transport of BL6B, UVSOR-II.

Ge/KBr, and quartz). The beamline layout is shown in Fig. 8. The IR/THz-SR focused by the 3D-MM is formed into a parallel beam by a collimator (M4) and is guided to the MP. When the parabolic mirror M3 is placed in the optical path, the IR/THz SR is guided to the MI. The IR/THz SR passing through the MP is guided to the reflection/absorption end-station (RAS) by a plane mirror (M8) in the switchyard #1. The light after the MI is guided to the micro-spectroscopy end-station (MSS) and the RAS by a plane mirror (M6) in the switchyard #2.

4.1 THz/IR reflection/absorption spectroscopy using SR

Figure 9 shows the optics of the RAS. Using the optics, both a reflection spectroscopy and transmission spectroscopy are available. The two experiments can be changed by adding a parabolic mirror $M_{RA}3$ without breaking the vacuum. Samples and all optical components are located in a high vacuum chamber ($\leq 10^{-6}$ Pa) evacuated by a turbo molecular pump (300 liter/s). There is no optical window in front of the samples. This has the advantages of no limitation of the photon energy and no interference by optical windows. An evaporator for gold film on the sample surface is added for measurement of absolute values. An automatic measurement system is also added to measure the relative intensity between the sample and a reference mirror at another
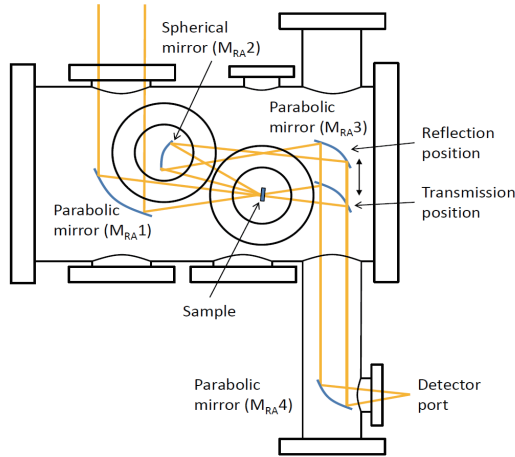
Fig. 9. Top-view of the optical path of the reflection/absorption end-station (RAS). The reflection/transmission experimental setup can be changed by moving the parabolic mirror $M_{RA}3$.

sample space. [10] The spectral distribution of IR/THz SR using RAS in the wavenumber region below 1000 cm^{-1} is shown in Fig. 10. The spectrum is covered down to $\sim$4 cm^{-1} ($\sim$0.13 THz) by using three kinds of combinations of light source (UVSOR-II), FTIR (FARIS-1 or Vertex 70v), and detector (InSb hot-electron bolometer or Si bolometer). The typical intensity in this region is about 100 times higher than thermal sources.

4.2 THz/IR micro-spectroscopy using SR

In the visible region, optical lenses are generally added for focusing. However, optical lenses cannot be used in the THz/IR region, because astigmatism appears: different refractive indexes occur because if the presence of impurities and many absorption lines from the lattice and molecular vibration modes. In the case of THz/IR, one mirror system consisting of one concave and one convex spherical mirror, namely Schwarzschild mirrors, is used (Fig. 11d). This system is used because it eliminates the astigmatism and gives high reflectivity in the THz/IR region due to Drude reflection of metals.

IR/THz SR is a powerful tool for micro-spectroscopy and imaging not only in the IR region but also in the THz region because of its high brilliance. Almost all of the world's IR/THz SR beamlines provide commercial IR microscopes that are easy to use. However, because the Schwarzschild mirrors in commercial IR microscopes are small (typically 2 inches in diameter), the microscopes are available only in the mid-IR region, *i.e.*, they are not

Frequency (THz)
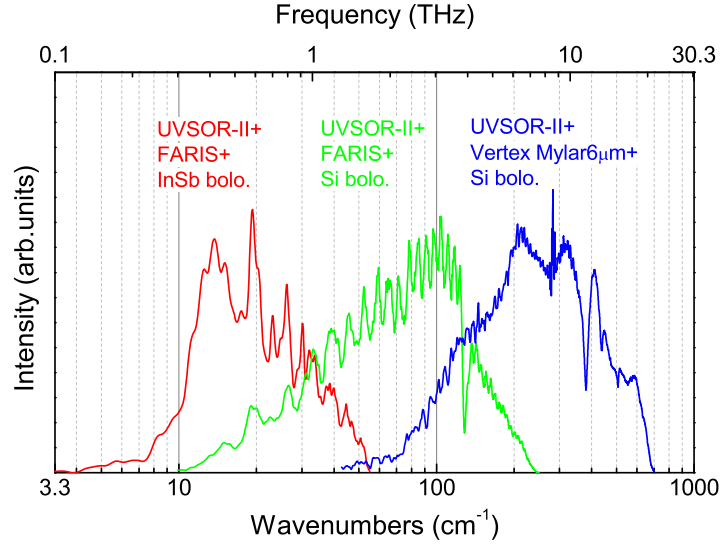
Fig. 10. Spectral distribution of the combination of light source (UVSOR-II), FTIR (FARIS-1 or Vertex 70v), and detector (InSb hot-electron bolometer or Si bolometer) in the THz region of BL6B, UVSOR-II. The lowest accessible wavenumber is about 4 cm^{-1} ($\sim$0.13 THz).

suitable for the THz region. However, we have installed a new microscope in order to cover the IR region and down to the THz region (Fig. 11). [12] Some of the main features are: 1) a large working distance, because experiments with specific requirements (at very low temperatures, under high pressures, for near-field spectroscopy, etc.) need to be performed; and 2) availability of the THz region, because the quasiparticle states of correlated materials and finger print vibration modes of proteins appear only in this spectral range. In order to achieve these goals, we use one set of large Schwarzschild mirrors (diameter = 140 mm, numerical aperture = 0.5, working distance = 106 mm, magnification = ×8) to reduce the diffraction effect in the THz region.

After installing of the THz microscope, we checked the spatial resolution in the different wavenumber ranges covered by the different FTIR beam splitters (Fig. 12). The spatial resolution was recorded by using a Bruker Vertex 70v interferometer and the transmission configuration. In the wavenumber region above 500 cm^{-1}, the globar lamp gives good contrast. However, the use of UVSOR-II increases the intensity by 10^2 and decreases the beam size by about 10 times. This implies that the brilliance of the IR/THz SR is 10^3 times higher than that of thermal sources. This is consistent with the brilliance measured at the first focusing point P1 (Fig. 8). If a pinhole 500 μm in diameter is installed at a counter focus position of the Schwarzschild mirror, the beam size becomes the diffraction limit. In the wavenumber region below 600 cm^{-1}, in which a
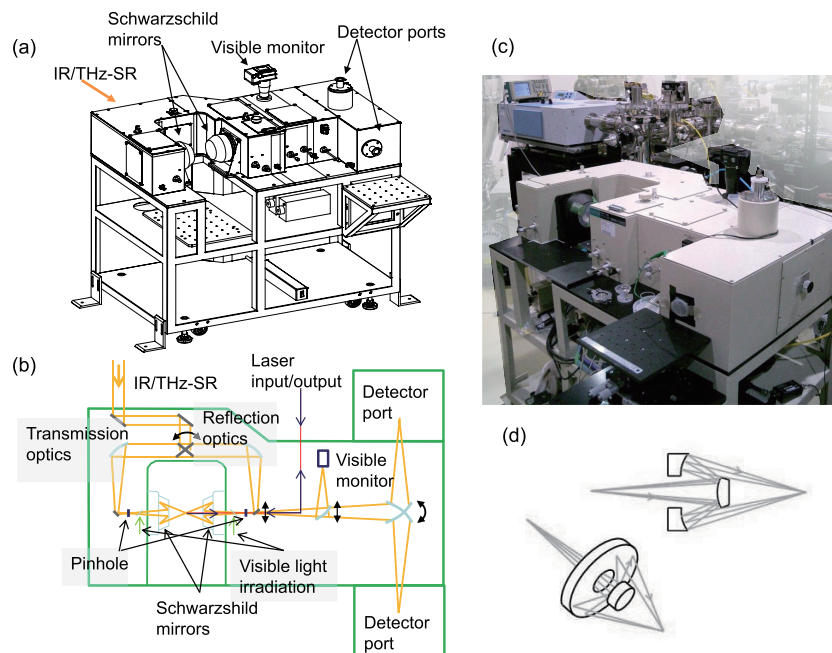
Fig. 11. 3D view of the THz micro-spectroscopy apparatus (a); top view of the optics (b), and photo (c) of the THz/IR micro-spectroscopy end-station (MSS) of the IR/THz beamline (BL6B) at UVSOR-II. (d) indicates the configuration of a Schwarzschild mirror.

Mylar 6-μm beam splitter is used, a good beam profile was observed with UVSOR-II, in contrast with the very weak peak given by a globar lamp. In addition, use of a Mylar 23-μm beam splitter covering the lower wavenumber region below 200 cm^{-1} gave good contrast and intensity in the peak image. The cut-off wavenumber for UVSOR-II is 40 cm^{-1} (150 cm^{-1} in the case of the SPring-8 IR beamline [11]). This indicates that the THz microscope using UVSOR-II is a very efficient tool for micro-spectroscopy in both the IR and the THz region. This instrument is used for electrodynamics studies of strongly correlated materials at low temperatures and under high pressures, and also for molecular vibration imaging of living cells.

## 5 Application of THz spectroscopy using SR: Temperature-dependent THz spectra of SmB$_6$

SmB$_6$, which is a typical Kondo semiconductor, has been studied over three decades. In the previous studies, two different energy gap sizes were proposed
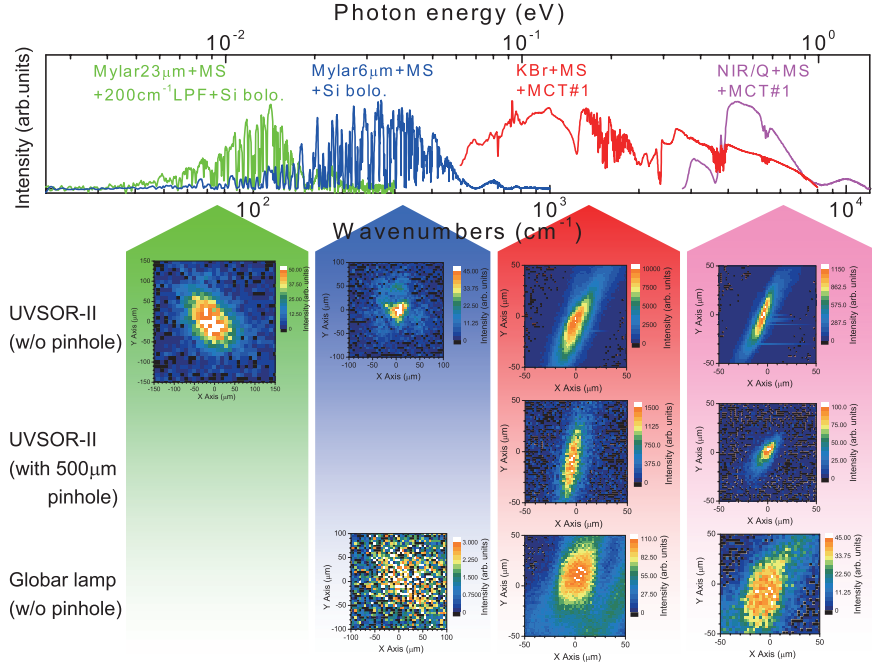
Fig. 12. Spectral distribution and spatial resolution of THz microscope at several wavenumber regions using UVSOR-II compared with a globar lamp. Labels in the top figure indicate the combinations of beam splitter of the FTIR (Bruker), low-pass filter, and detector. Labels on the left side indicate the light sources and apertures at other focuses of the Schwarzschild mirror. Fine structures in the spectral distributions are due to the absorption of water vapor and can be reduced by nitrogen purge. See the text for details.

one about 5 meV and the other about 15 meV [13]. However, a recent study using higher purity samples revealed that the lower energy absorption band originates from impurities, because the lower energy absorption becomes small with increasing purity [14, 15]. The higher energy gap is concluded to be intrinsic and to originate from hybridization between the localized Sm $4f$ state and the Sm $5d$ conduction band, so-called c-f hybridization [16]. In the case of c-f hybridization, a rigid band model suitably explains the physical properties. However, the specific heat curve cannot be explained by a rigid band model [17]. This means that there are temperature-dependent parameters in the electronic structure as well as in the charge dynamics.

On the other hand, the magnetic excitation at 14 meV increases with decreasing temperature below 20 K, as observed by using inelastic neutron scattering [18]. The magnetic excitation energy is similar to the energy gap observed in optical spectra. Therefore, if the c-f hybridization bands exist at
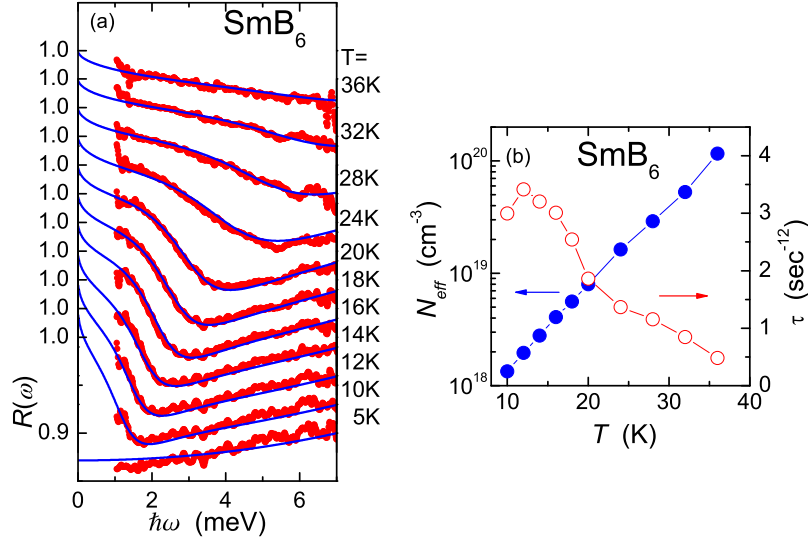
Fig. 13. (a) Temperature dependence of reflectivity spectrum of SmB_6 in the THz region (thick lines) and fitting functions by the combination of a Drude and two Lorentz functions (thin lines). Successive curves are offset by 0.03 for clarity. (b) Parameters obtained for the effective electron number (N_{eff}) and the relaxation time (τ) of the Drude function as a function of temperature.

the energy gap edge, the carriers should have the same temperature dependence. Optical reflection spectroscopy is good as a probe for investigating the character of carriers. In the case of SmB_6, the signal from the thermally excited carriers appears in the THz region. The change in the fitting parameters of the Drude function as a function of temperature must reflect the property at the energy gap edge. We therefore measured the temperature dependence of the reflectivity spectrum in the THz region.

The thick lines in Figure 13a show the temperature dependence of the reflectivity spectrum [$R(\omega)$] of SmB_6. At $T = 5$ K, the reflectivity does not approach unity with decreasing photon energy. This shows an insulating character. With increasing temperature, the reflectivity at the lower energy portion increases. The high reflectivity originates from the Drude component due to the presence of thermally excited carriers. The Drude component indicates the electronic structure of the thermally excited area near the energy gap edge.

The curves fitted by using one Drude and two Lorentz functions are indicated by the thin solid lines in Fig. 13a. The fitting function is as follows:

$$\hat{\varepsilon}(\omega) = \varepsilon_\infty - \frac{4\pi N_{eff}e^2}{m(\omega^2 - i\omega/\tau)} + \sum_{i=1}^{n} \frac{4\pi N_i e^2}{m\{(\omega_{i0}^2 - \omega^2) - i\omega/\tau_i\}}$$

$$R(\omega) = \left| \frac{1 - \hat{\varepsilon}(\omega)^{1/2}}{1 + \hat{\varepsilon}(\omega)^{1/2}} \right|^2$$

Here, $\hat{\varepsilon}(\omega)$, $\hat{n}(\omega)$ and $R(\omega)$ are a complex dielectric function, a complex refractive index and a reflectivity spectrum, respectively. ε_∞ is the sum of ε_1 above the measured energy region, N_{eff} and τ are the effective number and the relaxation time of the carriers, respectively, and m the rest mass of an electron. N_i, ω_{i0} and τ_i are the intensity, resonance frequency and relaxation time, respectively, of i-th bound state, including energy gaps in the electronic structure and optical phonons. The two Lorentz functions were set to the main gap at 15 meV and to the impurity state at 5 meV. The fitting functions reproduced the experimental curves well. The obtained N_{eff} and τ, derived from the fitting parameters, are shown as functions of temperature (Fig. 13b). If an activation type behavior [$N_{eff} \propto \exp(-2\Delta/k_{\mathrm{B}}T)$, where Δ is the energy gap and k_{B} is the Boltzmann constant] is expected, then $\log N_{eff}$ should be proportional to $1/T$. However, $\log N_{eff}$ is roughly proportional to T, as shown in Fig. 13b. This indicates that the energy gap cannot be explained by the rigid band model, but it may also indicate that the energy gap shrinks with increasing temperature. At two-state model could be assumed to explain this behavior [19]. On the other hand, τ rapidly increases on cooling below 20 K. This temperature is coincident with that of the growth of the magnetic excitation at 14 meV [18]. This means that thermal excitation of the carriers is strongly related to magnetic excitation at 14 meV.

6 Applications of THz micro-spectroscopy using SR

6.1 Experimental procedure of THz spectroscopy under high pressure

THz spectroscopy under high pressures has been performed by using the MSS, as shown in Fig. 14. To detect the charge dynamics, the optical reflection spectroscopy [$R(\omega)$] in the THz region must be performed, as mentioned in the previous section. High pressure is produced by using a diamond anvil cell (DAC). The experimental setup for reflection spectroscopy at high pressure and low temperature at MSS is shown in Fig. 14. Because the sample area in the pressure cell is smaller than 1 mm in diameter, we have to use a microscopic technique. THz spectroscopy under high pressures is difficult to perform using conventional FTIRs.

A membrane-type DAC (Diacell® OptDAC-LT, easyLab Technology Ltd.) was employed to produce high pressures on the samples. Figure 14c is a photo of the setup combined with the THz microscope. Pressure was applied to samples at low temperatures by using the He gas inlet to the membrane. Because the culet plane areas of diamond and of the membrane are 1.13 mm^2 and 1030 mm^2, respectively, the pressure on samples is about 10^3 times larger
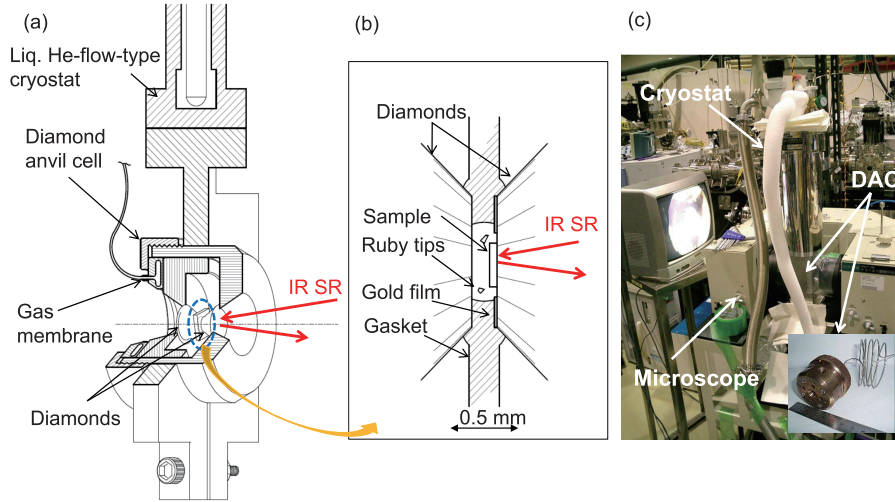
Fig. 14. Schematic figure of a diamond anvil cell (DAC) with a gas membrane combined with a liquid-helium-flow-type cryostat for reflection spectroscopy at high pressure and low temperature (a); the sample setup in the DAC (b); and photo of the experimental apparatus and the DAC (c).

than the helium gas pressure. The maximum pressure at the sample position is about 8 GPa. A sample with a typical size of $0.4 \times 0.4 \times 0.05$ mm^3 was set in a DAC with Apiezon-N grease as a pressure medium, with gold film as a reference and ruby tips for a pressure reference. The pressure was calibrated by ruby fluorescence measurement.

6.2 Electronic structure of SmS under high pressure

SmS is an insulator (the so-called "black phase") with a gap size of 1000 K ($\sim$80 meV) at ambient pressure [20]. Above about 0.7 GPa, the sample color changes to gold (golden phase) and the Sm-ion changes from divalence to mixed valence [21]. To investigate the mechanism of this transition, we performed THz reflection spectroscopy under pressure.

The $R(\omega)$ obtained for SmS at 300 K as a function of pressure is shown by the thick lines in Fig. 15a. At ambient pressure, the spectrum indicates an insulating one, because the low energy limit does not approach unity and a clear large peak due to the TO-phonon between the Sm^{2+} and S^{2-} ions appears. When pressure was applied, the background intensity increased with increasing pressure. The background indicates the appearance of carriers. Therefore, the carrier density increased with increasing pressure. The fitting curves of the combination of a Drude function and Lorentz functions are shown by the thin solid lines in the same figure. The Lorentz function was set to reproduce
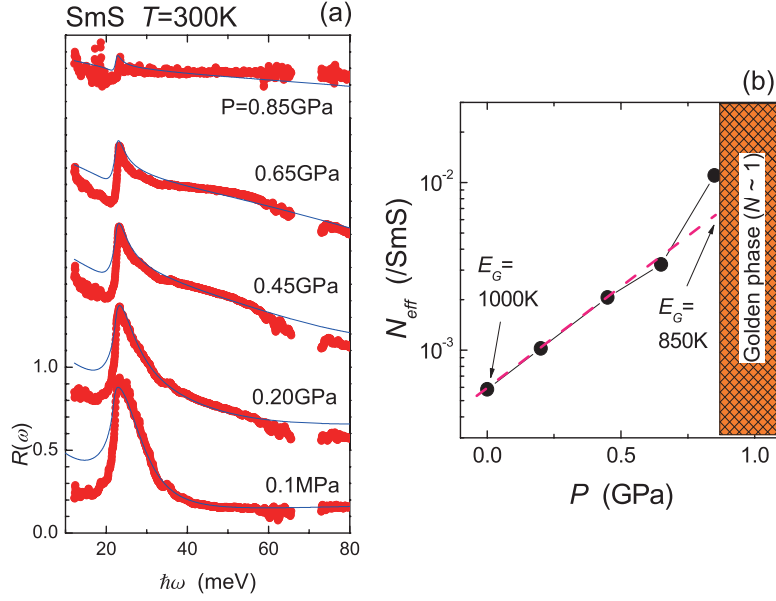
Fig. 15. (a) Pressure dependence of the reflectivity spectrum $[R(\omega)]$ of SmS (thick lines) in the black phase at 300 K. The fitting curves from the combination of a Drude and the Lorentz functions are plotted as thin solid lines. Successive curves are offset by 0.5 for clarity. (b) Pressure dependence of energy gap evaluated by Drude and Lorentz fitting of $R(\omega)$ spectra. See the text for details.

the TO-phonon. To fit the spectra obtained, only the N_{eff} in the Drude function is changed; all of the other parameters (τ in the Drude function and all parameters in the Lorentz function) are fixed. The N_{eff} obtained is plotted in Fig. 15b. The $\log N_{eff}$ is proportional to the pressure up to 0.65 GPa. This pressure dependence indicates that the energy gap closes with increasing pressure. The energy gap size (2Δ) at ambient pressure was evaluated to be about 1000 K [20]. By evaluating the gap size from N_{eff}, the energy gap at the black-golden phase boundary is 850 K; the gap then suddenly closes to 100 K in the golden phase by first-order transition [22].

7 Conclusion and outlook

In this paper, we have pointed out the high brilliance of the infrared (IR) and terahertz (THz) synchrotron radiation (SR) and have introduced the characteristic optics by which "three-dimensional magic mirror (3D-MM)" is used to focus the bending-magnet radiation. The 3D-MM is an ideal optical component for focusing bending-magnet radiation, because not only can the

synchrotron light be focused down to a diameter close to the electron beam size but also the time structure can be reduced to that of the electron beam length. Using 3D-MM, some advanced optical experiments have so far been performed (e.g. highly precise THz reflection spectroscopy, and THz spectroscopy at high pressure and low temperature). 3D-MM can also be used for time-resolved spectroscopy because of the conservation of the time structure of electron beams.

Recently, THz coherent SR (THz-CSR) has been developed in storage rings. THz-CSR, which is emitted when the electron beam length or the longitudinal structure is shorter than the wave length, has intensity several orders of magnitude higher than that of normal SR. The light has properties not only of high intensity but also full coherence. The light can be used for new experiments (e.g., THz-pump probe spectroscopy, and THz phase contrast imaging). Such new experiments will open up a new frontier in spectroscopy.

Acknowledgments

References

1. T. Nanba, Y. Urashima, M. Ikezawa, M. Watanabe, E. Nakamura, K. Fukui, and H. Inokuchi, Int. J. Infrared Millimeter Waves **7**, 759 (1986).
2. M. Katoh, M. Hosaka, A. Mochihashi, J. Yamazami, K. Hayashi, Y. Hori, T. Honda, K. Haga, Y. Takashima, T. Koseki, S. Koda, H. Kitamura, T. Hara, and T. Tanaka, AIP Conf. Proc. **705**, 49 (2004).
3. S. Kimura, E. Nakamura, T. Nishi, Y. Sakurai, K. Hayashi, J. Yamazaki, and M. Katoh, Infrared Phys. Tech. **49**, 147 (2006).
4. S. Kimura, E. Nakamura, J. Yamazaki, M. Katoh, T. Nishi, H. Okamura, M. Matsunami, L. Chen, and T. Nanba, AIP Conf. Proc. **705**, 416 (2004).
5. H. Kimura, T. Moriwaki, N. Takahashi H. Aoyagi, T. Matsushita, Y. Ishizawa, M. Masaki, S. Ohishi, H. Okuma, T. Nanba, M. Sakurai, S. Kimura, H. Okamura, N. Nakagawa, T. Takahashi, K. Fukui, K. Shinoda, Y. Kondo, T. Sata, M. Okuno, M. Matsunami, R. Koyanagi, and Y. Yoshimatsu, Nucl. Instrum. Meth. A **467-468**, 441 (2001).
6. T. Yaji, Y. Yamamoto, T. Ohta, and S. Kimura, Infrared Phys. Tech. **51**, 397 (2008).
7. J. D. Jackson, *Classical Electrodynamics, Third Edition* (John Wiley & Sons, Inc., 1999).
8. R. Lopez-Delgado and H. Szwarc, Opt. Commun. **19**, 286 (1976).

9. S. Kimura, H. Kimura, T. Takahashi, K. Fukui, Y. Kondo, Y. Yoshimatsu, T. Moriwaki, T. Nanba, and T. Ishikawa, Nucl. Instrum. Meth. A **467-468**, 437 (2001).
10. S. Kimura, JASCO Report **50**, 6 (2008). [in Japanese]
11. Y. Ikemoto, T. Moriwaki, T. Hirono, S. Kimura, K. Shinoda, M. Matsunami, N. Nagai, T. Nanba, K. Kobayashi, and H. Kimura, Infrared Phys. Tech. **45**, 369 (2004).
12. S. Kimura, Y. Sakurai, E. Nakamura, and T. Mizuno, AIP Conf. Proc. **879**, 595 (2006).
13. G. Travaglini and P. Wachter, Phys. Rev. B **29**, 893 (1984).
14. T. Nanba, H. Ohta, M. Motokawa, S. Kimura, S. Kunii, and T. Kasuya, Physica B **186-188**, 440 (1993).
15. S. Kimura, T. Nanba, S. Kunii, and T. Kasuya, Phys. Rev. B **50**, 1406 (1994).
16. G. Aeppli and Z. Fisk, Comments Condens. Matter Phys. **16**, 155 (1992).
17. T. Kasuya, K. Takegahara, Y. Aoki, K. Hanzawa, M. Kasaya, S. Kunii, T. Fujita, N. Sato, H. Kimura, T. Komatsubara, T. Furuno, and J. Rossat-Mignod, *Valence Fluctuation in Solids, p.* 215, (North-Holland, 1981).
18. P.A. Alekseev, J.M. Mignot, J. Rossat-Mignod, V.N. Lazukov, I.P. Sadikov, E.S. Konovalova, and Yu.B. Paderno, J. Phys.: Condens. Matter **7**, 289 (1995).
19. B. Gorchunov, N. Sluchanko, A. Volkov, M. Dressel, G. Knebel, A. Loidl, and S. Kunii, Phys. Rev. B **59**, 1808 (1999).
20. K. Matsubayashi, K. Imura, H.S. Suzuki, T. Mizuno, S. Kimura, T. Nishioka, K. Kodama, and N.K. Sato, J. Phys. Soc. Jpn. **76**, 064601 (2007).
21. J.L. Kirk, K. Vedam, V. Narayanamurti, A. Jayaraman, and E. Bucher, Phys. Rev. B **6**, 3023 (1972).
22. T. Mizuno, S. Kimura, K. Matsubayashi, K. Imura, H.S. Suzuki, and N.K. Sato, J. Phys. Soc. Jpn. **77**, 113704 (2008).